JOURNAL OF MATERIALS SCIENCE 20 (1985) 97–104

Production of Ni–Pd–Si and Ni–Pd–P amorphous wires and their mechanical and corrosion properties

A. INOUE
The Research Institute for Iron, Steel and Other Metals, Tohoku University, Sendai 980, Japan

Y. MASUMOTO
Sailor Pen Co. Ltd, Kure 731-44, Japan

N. YANO
Unitika Research and Development Centre, Unitika Ltd, Uji 611, Japan

A. KAWASHIMA, K. HASHIMOTO, T. MASUMOTO
The Research Institute for Iron, Steel and Other Metals, Tohoku University, Sendai 980, Japan

Wire-shaped nickel-based amorphous alloys exhibiting high strength and good ductility combined with a high corrosion resistance were produced for Ni–Pd–Si and Ni–Pd–P alloys by melt spinning in rotating water. The amorphous wires were formed over a relatively wide range from 29 to 82 at % palladium for $(\mathrm{Ni{-}Pd})_{82}\mathrm{Si}_{18}$ alloys and from 12 to 52 at % palladium for $(\mathrm{Ni{-}Pd})_{80}\mathrm{P}_{20}$ alloys. The Ni–Pd–metalloid amorphous wires had a circular cross-section and smooth surface, and their diameters were 80 to 150 μm. With increasing nickel content, their tensile strength, σ_f, increased from 1340 to 1710 MPa and the elongation to fracture, ϵ_f, decreased slightly from 2.2% to 1.9%. Cold-drawing the wires was an easy technique to reduce their diameter and to increase σ_f and ϵ_f up to an appropriate value of reduction in diameter. In addition, it is also effective in smoothing the wire surface. Their corrosion resistance was assumed to be sufficiently high since their polarization behaviour in 1 N H_2SO_4 solution was similar to palladium metal. Cold-drawing did not enhance corrosion and rather decreased apparently the active dissolution current density of some alloys owing to smoothing of the surface.

1. Introduction

A number of alloys such as (Fe, Co, Ni, Pd or Pt)–(B, P, C, and/or Si) [1–3] and Cu–Zr [4] are able to form single-phase amorphous ribbons thicker than 100 μm on melt spinning. Almost all of them become continuous amorphous wires of 70 to 250 μm diameter on melt spinning in rotating water [5–9]. Application of this in-rotating-water spinning technique to Ni–Si–B ternary alloys, however, results in a complete destruction of the alloy jet stream ejected in rotating water, with the consequent formation of amorphous powders of 50 to 150 μm diameter [10], instead of amorphous wires. Since the Ni–Si–B alloys possess a large amorphous phase-forming ability comparable to Fe–Si–B ternary alloys [1, 2], factors other than the amorphous phase-forming ability must be taken into account for the production of wire-shaped amorphous alloys.

The production of nickel-based amorphous wires is strongly desirable from an engineering point of view, since the wires are expected to have high resistance to mechanical and thermal embrittlement as well as good corrosion resistance.

0022–2461/85 $03.00 + .12 © 1985 Chapman and Hall Ltd.

Recently, nickel-based amorphous alloy wires were successfully prepared by melt-spinning in rotating water for Ni–Pd alloys containing silicon or phosphorus, which enhances significantly the viscosity of the liquid [6, 10]. This paper aims to clarify the composition range and quenching conditions for the formation of Ni–Pd–Si and Ni–Pd–P amorphous alloy wires and to examine their mechanical properties and corrosion behaviour.

2. Experimental methods

The specimens used were $Ni_{100-x-y}Pd_xSi_y$ and $Ni_{100-x-y}Pd_xP_y$ ternary alloys. Crystalline Ni–Pd–Si ingots were first cast into rod-shaped ingots by induction melting of electrolytic nickel plates and palladium and silicon chips in a flowing argon atmosphere. The Ni–Pd–P ingots were prepared as follows: prescribed amounts of palladium chips, nickel powder and red phosphorus were vaccum-sealed in a quartz ampoule after mixture, and the reaction of phosphorus with nickel and palladium was carried out at about 600 K for 12 h and then the temperature was gradually raised to melt the nickel–palladium phosphide for homogenization. The compositions were expressed by the intended values in atomic per cent since the difference between intended and chemically analysed compositions was less than 0.10 wt% for silicon and 0.14 wt % for phosphorus.

Amorphous wires of various diameters between 0.08 and 0.15 mm were prepared from small pieces of the master ingots by an in-rotating-water spinning apparatus in which the melt was ejected through the orifice into the rotating water layer. Details of the apparatus were described elsewhere [8, 11]. Typically, the amount of alloy melted was about 1 g, the rotational speed of the drum (50 cm diameter) was controlled in the range 290 to 320 rpm and the depth of the cooling water was about 25 mm. As reference samples, ribbon specimens ~1.5 mm wide and 0.03 mm thick were prepared by directing a stream of molten alloy on to the outer surface of a rapidly revolving copper roller.

Identification of the as-quenched phases was made using diffractometer X-ray method using Cu*Kα* radiation in combination with an X-ray monochrometer as well as by optical microscopy and differential scanning calorimetry (DSC). The wires and ribbons were determined to be amorphous when the X-ray diffraction pattern showed a typical liquid-like structure. The tensile strength of the wires was measured by an Instron-type tensile testing machine at a strain rate of $4.7 \times 10^{-4} sec^{-1}$. Specimens for the tensil test were cut for as-cast and cold-drawn long wires into short pieces having a gauge dimension of 20 mm length. A specially designed set of grips for the small filament were used to ensure proper specimen alignment within the machine. Peripheral fracture appearance was observed using a scanning electron microscope.

The evaluation of corrosion resistance was made by measuring potentiodynamic polarization curves in 1 N H_2SO_4 solution at room temperature with a potential sweep rate of $2.4 \times 10^{-3} V sec^{-1}$, starting from the corrosion potential. Immediately before polarization measurements, the wire specimens were mechanically polished with silicon carbide paper to no. 2000 in cyclohexane and were then cathodically reduced at a constant current density of $10 A m^{-2}$ for 5 min in the sulphuric acid.

3. Results and discussion

3.1. Formation ranges of the amorphous wires

Fig. 1 shows the concentration range of palladium, x, in $(Ni_{1-x}Pd_x)_{80}P_{20}$ and $(Ni_{1-x}Pd_x)_{82}Si_{18}$ alloys which were vitrifiable in the shape of wire of about 100 μm diameter as well as ribbon. The main quenching parameters for melt spinniing in rotating water, such as the distance from the surface of water to the end of the quartz tube, the nozzle size, the ejecting pressure, the temperature of the melt, the temperature of cooling water and the ratio of the water velocity to the drum velocity, were adjusted to be almost the same for Pd–Cu–Si [8], Fe–Si–B [5], Fe–P–C [6] and Co–Si–B [7] amorphous wires. Whilst the amorphous ribbons are formed over the whole

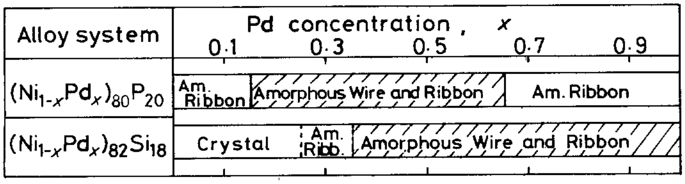

Figure 1 Composition ranges of $(Ni_{1-x}Pd_x)_{80}P_{20}$ and $(Ni_{1-x}Pd_x)_{82}Si_{18}$ ternary alloys for the formation of amorphous wires of about 100 μm diameter and amorphous ribbons of about 30 μm thickness.

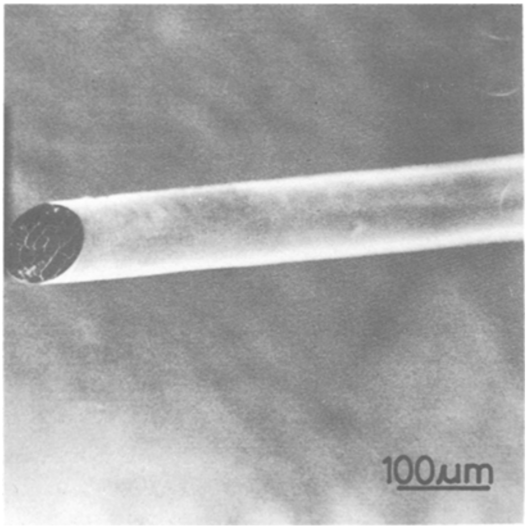

Figure 2 Scanning electron micrograph of as-quenched $(Ni_{0.8}Pd_{0.2})_{80}P_{20}$ amorphous wire.

composition range in the Ni–Pd–P alloys and in the range $x = 0.25$ to 1.0 in the Ni–Pd–Si alloys, the formation of the wire is limited to a narrower range from $x = 0.15$ to 0.65 for the Ni–Pd–P alloys and from $x = 0.35$ to 1.0 for the Ni–Pd–Si alloys. The compositional limitation of amorphous wire formation is possibly due to the decrease in the amorphous phase-forming ability because, just outside the limitation, the brittle wires were apt to form having a duplex structure consisting of amorphous and crystalline phase. The metalloid contents suitable for the formation of nickel-based amorphous wires are in the range 17 to 25 at % phosphorus for $(Ni_{0.7}Pd_{0.3})_{100-x}P_x$ and 16 to 22 at % silicon for $(Ni_{0.6}Pd_{0.4})_{100-x}Si_x$ alloys.

Fig. 2 shows a scanning electron micrograph of the $(Ni_{0.8}Pd_{0.2})_{80}P_{20}$ amorphous wire, which contains the largest amount of nickel in the present work. The thickness variation measured by the micrometer gauge was less than 10% of approximately 120 µm diameter for the wire shown in Fig. 2 and was liable to decrease with decreasing diameter. Thus, the nickel-based amorphous wires produced by this technique possess a good uniformity of shape. This fact indicates that the molten jet stream was quite stable in rotating water and was supercooled without any destruction of the stable jet stream below the glass transition temperature, T_g, of the alloy even in a moving liquid medium, such as rotating water. This is in marked contrast to the previous results [10] when the application of the present melt-spinning technique to Ni–Si–B ternary and Ni–Pd–Si–B quaternary alloys resulted in a complete destruction of the jet stream before supercooling to T_g, and hence led to the formation of amorphous powders of 50 to 150 µm diameter. It is, therefore, reasonable to conclude that a large amount of dissolution of phosphorus or silicon in nickel-base alloys and/or the elimination of boron significantly raise the stability of the molten jet stream in the rapidly rotating water layer, probably because of the remarkable increase in the viscosity of the liquid.

3.2. Mechanical properties and fracture morphology

The tensile fracture strength (σ_f), and fracture elongation (ϵ_f) including elastic elongation of Ni–Pd–Si and Ni–Pd–P amorphous wires in as-cast and cold-drawn states are summarized in Table I, where the glass transition temperature, T_g, crystallization temperature, T_x, wire diameter before drawing and reduction in wire cross-sectional area by drawing (R) are also given. The strength values are the average of seven specimens and T_x is the onset temperature of crystallization determined from the DSC curve obtained at a heating rate of 40 K min^{-1}. As seen in the table, σ_f of the as-cast wires tends to increase from 1340 to 1710 MPa with increasing nickel content, while ϵ_f of Ni–Pd–Si wires decreases from 2.2% to

TABLE I Tensile fracture strength (σ_f), elongation to fracture (ϵ_f) including elastic elongation, glass transition temperature (T_g), crystallization temperature (T_x) and wire diameter (D) for Ni–Pd–Si and Ni–Pd–P amorphous wires in as-cast and cold-drawn states. R is the reduction in cross-sectional area by drawing

Alloy composition	σ_f (MPa)	ϵ_f (%)	T_g (K)	T_x (K)
$(Ni_{0.6}Pd_{0.4})_{82}Si_{18}$				
$D = 121$ µm	1710	2.0	–	674
$R = 56\%$	2030	2.7	–	–
$(Ni_{0.4}Pd_{0.6})_{82}Si_{18}$				
$D = 92$ µm	1560	1.9	676	698
$R = 25\%$	1890	2.7	–	–
$(Ni_{0.2}Pd_{0.8})_{82}Si_{18}$				
$D = 86$ µm	1340	1.9	680	705
$R = 32\%$	1650	2.9	–	–
$(Ni_{0.1}Pd_{0.9})_{82}Si_{18}$				
$D = 106$ µm	1490	2.2	664	692
$R = 22\%$	1580	3.1	–	–
$(Ni_{0.4}Pd_{0.6})_{80}P_{20}$				
$D = 88$ µm	1440	2.2	583	601
$R = 22\%$	1680	3.1	–	–

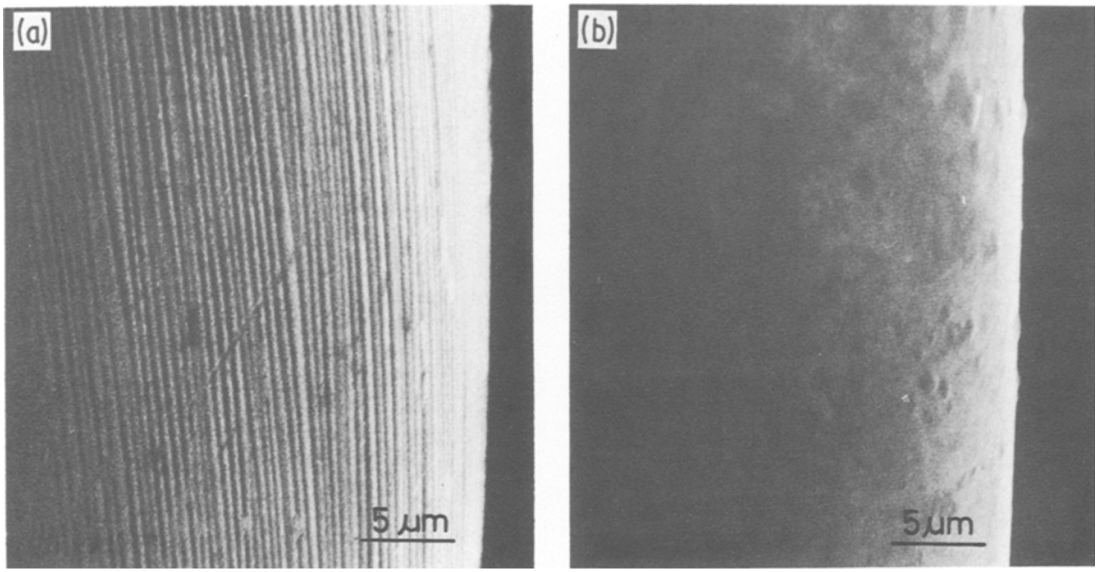

Figure 3 Scanning electron micrographs of as-cast and cold-drawn (57% reduction in diameter) wires of amorphous $(Ni_{0.4}Pd_{0.6})_{82}Si_{18}$ alloy.

1.9%, although σ_f for $(Ni_{0.1}Pd_{0.9})_{82}Si_{18}$ alloys and ϵ_f for $(Ni_{0.6}Pd_{0.4})_{82}Si_{18}$ alloys are exceptional. The table also shows that complete replacement of silicon by phosphorus results in a decrease in σ_f by about 9% and an increase in ϵ_f by about 14%. In both the alloy systems, there is no appreciable sample diameter effect on the value of σ_f in the diameter range 80 to 150 µm, but ϵ_f increases by about 12% with increasing wire diameter from 80 to 150 µm for $(Ni_{0.1}Pd_{0.9})_{82}Si_{18}$ wires. The effect of sample size on σ_f and ϵ_f is similar to that for Fe–Si–B amorphous wires [5].

Next, the total limit of area of reduction of the Ni–Pd–Si and Ni–Pd–P amorphous wires by cold drawing was examined, which is a very important factor for practical applications. All the amorphous wires produced in the present work would be cold-drawn from 0.12 mm to 0.03 mm diameter after multiple passings through appropriate diamond dies without annealing treatments. Soapy water was used as a lubricant in the cold drawing. All the Ni–Pd–Si and Ni–Pd–P amorphous wires possess a good bending ductility, even after cold drawing as severe as about 75% reduction in cross-sectional area. Magnified scanning electron micrographs clearly revealed the difference in surface roughness between as-cast and cold-drawn wires, as shown, for example, in Fig. 3. The as-cast wire was finely uneven since the alloy liquid jet was solidified in contact with the water stream. The uneveness was hardly eliminated by mechanical polishing with silicon carbide paper but was almost completely removed by cold drawing. Consequently, the cold drawing is effective in smoothing the amorphous wire surface.

As is seen in Table I, both σ_f and ϵ_f increase significantly on cold drawing up to an appropriate reduction in area. As an example, the stress–elongation curves of $(Ni_{0.1}Pd_{0.9})_{82}Si_{18}$ amorphous wires (original diameter $\simeq$ 106 µm) before and after drawing are shown in Fig. 4. Changes in σ_f and ϵ_f before and after drawing for $(Ni_{1-x}Pd_x)_{82}Si_{18}$ and $(Ni_{0.4}Pd_{0.6})_{80}P_{20}$ amorphous wires possessing the original diameter of about 120 µm, are shown in Figs. 5 and 6 as a function of the total reduction in cross-sectional area. The general features of these figures are summarized below.

1. σ_f and ϵ_f increase gradually with increasing reduction in area, reach a maximum value at an appropriate reduction per cent and tend to decrease with further reduction in area. In addition, the reduction ratio where σ_f and ϵ_f exhibit maxima tends to increase with increasing nickel content.

2. Young's modulus, E, decreases by about 8.7% upon cold drawing, even though the determination of E from the gradient of the stress–elongation curve is not always approriate.

3. The maximum σ_f values of the wires drawn to an optimum reduction in area exhibit a clear

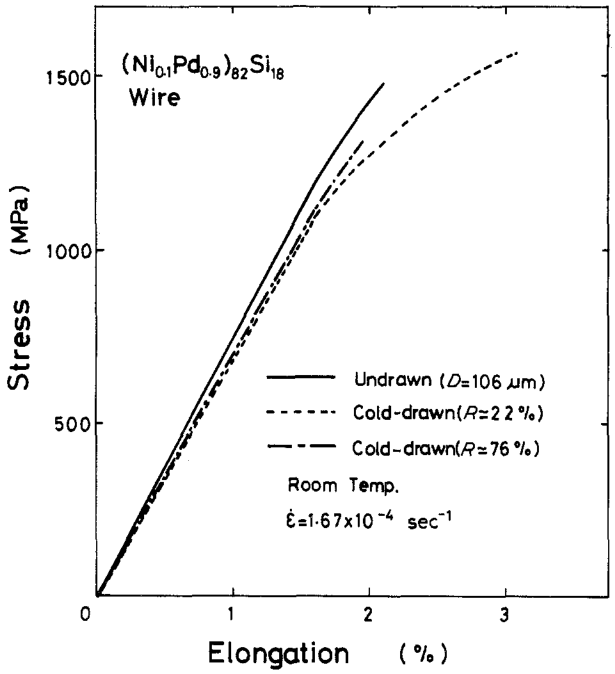

Figure 4 Stress–elongation curves of as-cast and cold-drawn $(Ni_{0.1}Pd_{0.9})_{82}Si_{18}$ amorphous wires.

compositional dependence and increase systematically with increasing nickel content. The highest σ_f value attained is 2030 MPa at $R = 56\%$ for $(Ni_{0.6}Pd_{0.4})_{82}Si_{18}$, which greatly exceeds the highest value (1290 MPa) [13] for the conventional nickel-based crystalline alloys.

4. The Ni–Pd–Si alloys exhibit higher σ_f and lower ϵ_f than those of the Ni–Pd–P alloys in both as-cast and drawn states, in spite of the lower metalloid content.

The tensile fracture appearance of the as-cast $(Ni_{0.6}Pd_{0.4})_{82}Si_{18}$ and $(Ni_{0.8}Pd_{0.2})_{80}P_{20}$ amorphous wires is shown in Figs. 7a and b. It is seen that tensile fracture occurs on a shear plane at 45° to 50° to the transverse direction of the wire and the morphology of the fracture surface is composed

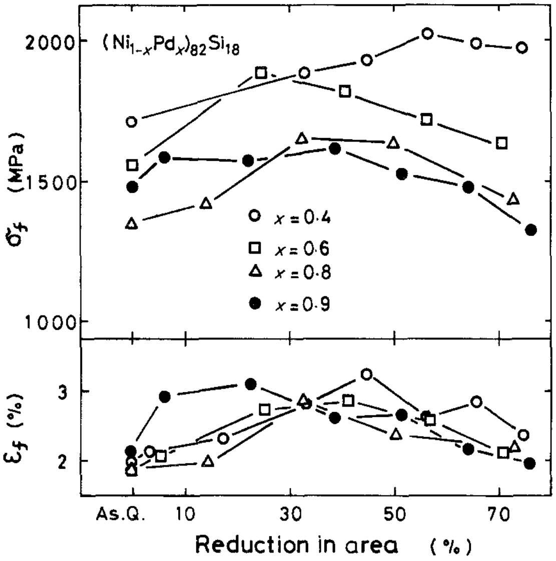

Figure 5 Changes in tensile strength (σ_f) and elongation to fracture (ϵ_f) of $(Ni_{1-x}Pd_x)_{82}Si_{18}$ amorphous wires with reduction in area.

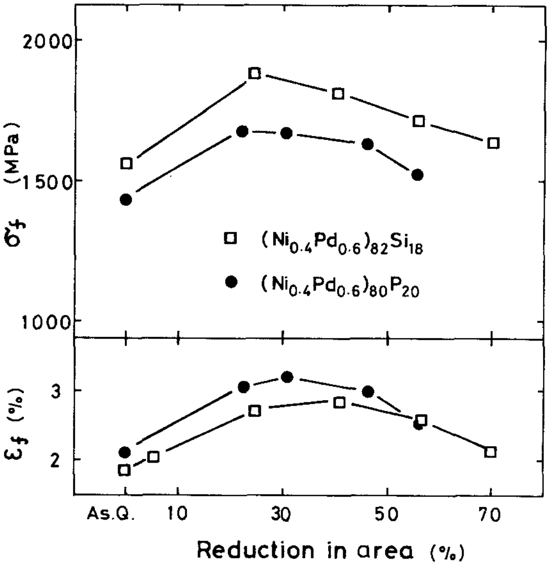

Figure 6 Changes in tensile strength (σ_f) and elongation to fracture (ϵ_f) of $(Ni_{0.4}Pd_{0.6})_{82}Si_{18}$ and $(Ni_{0.4}Pd_{0.6})_{80}P_{20}$ amorphous wires with reduction in area.

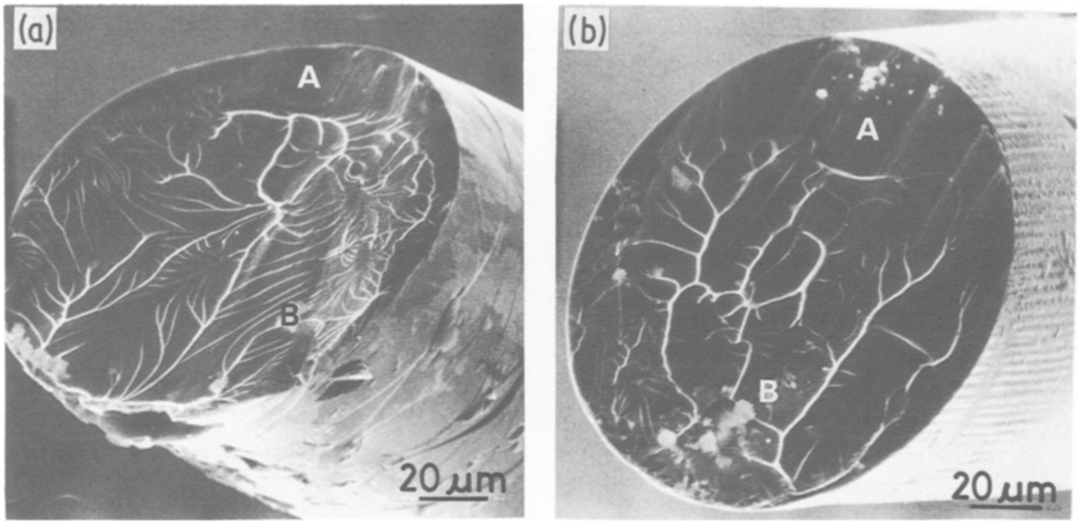

Figure 7 Scanning electron micrographs of the fracture surfaces obtained by tensile failure of (a) as-cast $(Ni_{0.6}Pd_{0.4})_{82}$-Si_{18} and (b) $(Ni_{0.8}Pd_{0.2})_{80}P_{20}$ amorphous wires.

of two distinguishable zones. One is a relatively featureless zone (A) produced by shear slip, and the other (B) is a vein pattern produced by the rupture of the cross-section remaining after the initial shear displacement. The features of the fracture appearance for the Ni–Pd–Si and Ni–Pd–P wires are independent of alloy composition and remain unchanged after cold drawing. Furthermore, one can see in Figs. 7a and b that the fraction of the featureless zone which occurred by shear displacement prior to final failure is larger for Ni–Pd–P than for Ni–Pd–Si. This suggests the possibility that the ductile nature of the Ni–Pd–P wire is superior to the Ni–Pd–Si wire, being consistent with the result of tensile fracture strain.

3.3. Corrosion behaviour

Potentiodynamic anodic polarization curves of amporphous $(Ni_{1-x}Pd_x)_{82}Si_{18}$ wires measured in 1 N H_2SO_4 solution at 303 K are shown in Fig. 8. Because it was difficult to vitrify binary Ni–Si alloys by melt spinning, the polarization curve of amorphous $Ni_{78}Si_{10}B_{12}$ alloy ribbon is added to the figure for comparison together with crystalline palladium and nickel metals. The polarization behaviour of the amorphous wires is almost the same as that of crystalline palladium metal show-

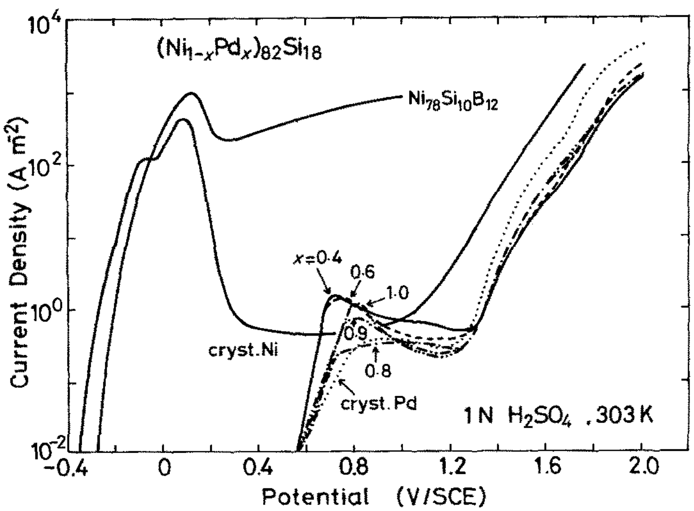

Figure 8 Potentiodynamic anodic polarization curves of amorphous $(Ni_{1-x}$-$Pd_x)_{82}Si_{18}$ alloy wires, amorphous Ni_{78}-$Si_{10}B_{12}$ alloy ribbon and crystalline nickel and palladium metals measured in 1 N H_2SO_4 solution.

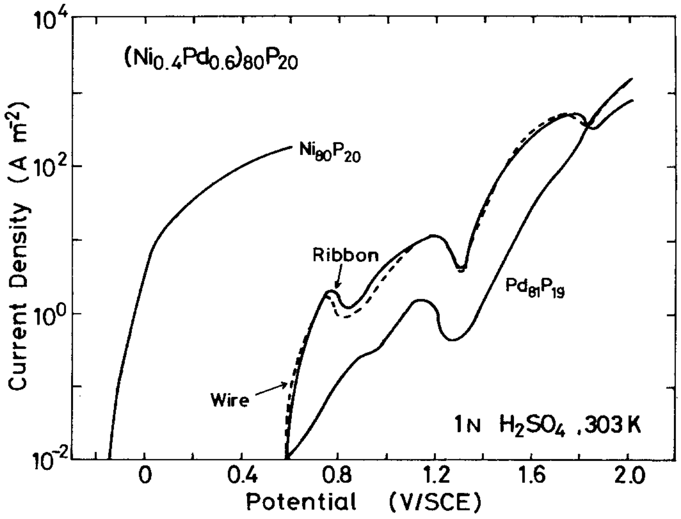

Figure 9 Potentiodynamic anodic polarization curves of as-cast wire and ribbon of amorphous $(Ni_{0.4}Pd_{0.6})_{80}P_{20}$ alloy and amorphous $Ni_{80}P_{20}$ and $Pd_{81}P_{19}$ alloy ribbons measured in 1 N H_2SO_4 solution.

ing the characteristics of noble metal, while the amorphous $Ni_{78}Si_{10}B_{12}$ alloy dissolved actively in a low potential region and was hardly passivated. The corrosion potential of the amorphous wires is not different from that of the palladium metal, although their current densities in the active region are higher than the palladium metal. The maximum current density in the active region is lowest at the palladium content x of 0.8 and raised with either increase or decrease in palladium content. The beneficial effect of alloying addition of a second metallic element in improving the corrosion resistance of amorphous metal–metalloid alloys is illustrated elsewhere [14].

Fig. 9 shows potentiodynamic polarization curves of amorphous $(Ni_{0.4}Pd_{0.6})_{80}P_{20}$ alloy ribbon and wire along with those of amorphous $Ni_{80}P_{20}$ and $Pd_{81}P_{19}$ alloy ribbons. The polarization curve of the wire is nearly the same as that of the ribbon-shaped counterpart. Their corrosion potentials are nearly the same as those of amorphous $Pd_{81}P_{19}$ alloy and crystalline palladium metal, and their polarization behaviour is different from amorphous $Ni_{80}P_{20}$ alloy and is largely affected by palladium although their anodic current densities are higher than those of the amorphous $Pd_{81}P_{19}$ alloy and crystalline palladium metal. Up to the primary current maximum their anodic current densities are almost the same as those of the amorphous $(Ni_{0.4}Pd_{0.6})_{82}Si_{18}$ wire, and hence the open circuit corrosion rate in acidic solutions may not be effected by change of metalloid.

An interesting result was obtained after cold-drawing. As shown in Fig. 10, cold-drawing the

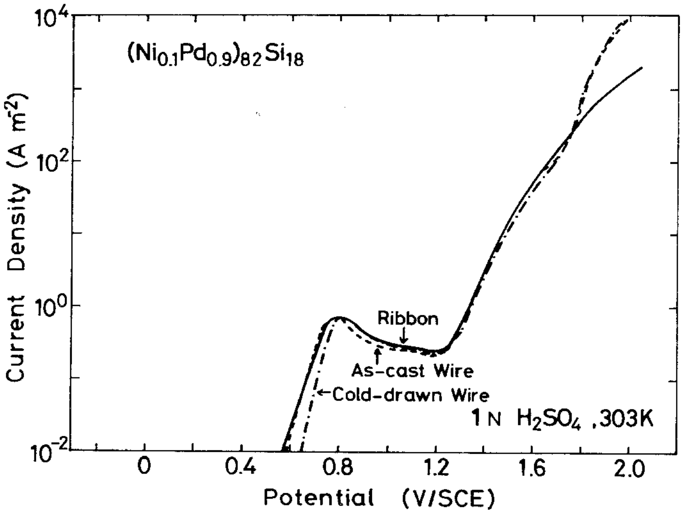

Figure 10 Potentiodynamic anodic polarization curves of as-cast and cold-drawn (52% reduction in diameter) wires and ribbon of amorphous $(Ni_{0.1}Pd_{0.9})_{82}Si_{18}$ alloy measured in 1 N H_2SO_4 solution.

amorphous $(Ni_{0.1}Pd_{0.9})_{82}Si_{18}$ wire ennobled the corrosion potential and decreased the anodic current density up to the current maximum. In this connection enhanced corrosion was observed along slip steps during chemical etching of plastically deformed amorphous $Pd_{77.5}Cu_6Si_{16.5}$ [15] and $Ni_{45}Pd_{35}P_{20}$ [16] alloys. On the other hand, Devine [17] found no enhanced corrosion at slip steps of amorphous $Ni_{35}Fe_{30}Cr_{15}P_{14}B_6$ alloy plastically bent to a total strain of 3.6% but observed a marked increase in the corrosion rate due to crevice corrosion at the intersections of surface microcracks after cold-rolling the material to 32% reduction in thickness. In contrast to these findings, cold-drawing the amorphous Ni–Pd–Si wires ennobled the corrosion potential and decreased the current density for active dissolution. As shown in Fig. 3, cold-drawing the Ni–Pd–metalloid wires did not induce detectable surface microcracks and resulted in smoothing rather than roughening of the surface. In the potential region where the cathodic current is based on a limiting diffusion of dissolved oxygen, a decrease in surface roughness is particularly effective in lowering the apparent anodic dissolution current density. In conclusion, cold-drawing does not enhance the active dissolution of amorphous Ni–Pd–metalloid wires in strongly acidic solutions, and is rather effective in smoothing the amorphous wire surface.

4. Conclusion

Wires of nickel-rich amorphous alloys were prepared for Ni–Pd–Si and Ni–Pd–P alloys having a high ability of amorphous plase formation and showing high mechanical strength and good ductility as well as high corrosion resistance. The production of amorphous wires was carried out by melt spinning in roatating water. The formation ranges of the amorphous wires were from 29 to 82 at% palladium for $(Ni–Pd)_{82}Si_{18}$ and 12 to 52 at% Pd for $(Ni–Pd)_{80}P_{20}$. The diameter of the Ni–Pd amorphous wires ranges from 80 to 150 μm. The wires were characterized by a circular cross-section and smooth surface. Increasing the nickel content improved the tensile strength, σ_f, and decreased the elongation to fracture, ϵ_f, including elastic elongation. The Ni–Pd–Si wires possessed higher σ_f and lower ϵ_f than the Ni– Pd–P wires. By cold-drawing to an appropriate reduction in area, σ_f and ϵ_f of Ni–Pd–Si amorphous wires increased by about 20% and 60%, respectively, and the highest σ_f and ϵ_f values attained were 2030 MPa and 2.2% for $(Ni_{0.6}Pd_{0.4})_{82}Si_{18}$. The strengths of the cold-drawn wires greatly exceeded the highest value of the conventional nickel-based alloys. The polarization behaviour of the amorphous wires in 1 N H_2SO_4 solution was similar to palladium metal, suggesting a high corrosion resistance. It is noteworthy that cold-drawing the wires did not accelerate corrosion in the strongly acidic solution and rather led to a decrease in the active dissolution current of some alloys due to smoothing of the surface. Thus, the Ni–Pd–Si and Ni–Pd–P amorphous wires are very attractive because of their high ability to form an amorphous wire, of circular cross-section, and high strength combined with good ductility, good corrosion resistance and inexpensiveness, and are expected to be used practically as the tip material in various kinds of brushes and pens.

References

1. M. HAGIWARA, A. INOUE and T. MASUMOTO, *Met. Trans.* **12A** (1981) 1027.
2. *Idem, Sci. Rep. Res. Inst. Tohoku Univ.* **A-29** (1981) 351.
3. H. S. CHEN and E. COLEMAN. *J. Appl. Phys. Lett.* **28** (1976) 245.
4. A. INOUE, N. YANO and T. MASMUMOTO, *J. Mater. Sci.* **19** (1984) 3786.
5. M. HAGIWARA, A. INOUE and T. MASUMOTO, *Met. Trans.* **13** (1982) 373.
6. A. INOUE, M. HAGIWARA and T. MASUMOTO, *J. Mater. Sci.* **17** (1982) 580.
7. M. HAGIWARA, A. INOUE and T. MASUMOTO, *Mater. Sci. Eng.* **54** (1982) 197.
8. T. MASUMOTO, I. OHNAKA, A. INOUE and M. HAGIWARA, *Scripta Metall.* **15** (1981) 293.
9. A. INOUE, H. S. CHEN, J. T. KRAUSE, T. MASUMOTO and M. HAGIWARA, *J. Mater. Sci.* **18** (1983) 2743.
10. T. MASUMOTO, A. INOUE, M. HAGIWARA, I. OHNAKA and T. FUKUSAKO, Proceedings of the 4th International Conference on Rapidly Quenched Metals, Vol. 1, edited by T. Masumoto and K. Suzuki, (The Japan Institute of Metals, Sendai, 1982) p. 47.
11. I. OHNAKA, T. FUKUSAKO and T. DAIDO, *J. Japan Inst. Metals* **45** (1981) 751.
12. H. S. CHEN, *Acta Metall.* **22** (1974) 1505.
13. "Metals Databook" (Japan Institute of Metals, 1974) p. 171.
14. K. HASHIMOTO, K. ASAMI, M. NAKA and T. MASUMOTO, *Corros. Sci.* **19** (1979) 857.
15. C. A. PAMPILLO, *Scripta Metall.* **6** (1972) 915.
16. S. TAKAYAMA and R. MADDIN, *Acta Metall.* **23** (1975) 943.
17. T. M. DEVINE, *J. Electrochem. Soc.* **124** (1977) 38.

*Received 23 February
and accepted 9 March 1984*